


CO₂ Reduction Hot Paper
How to cite: *Angew. Chem. Int. Ed.* **2023**, *62*, e202218039

International Edition: doi.org/10.1002/anie.202218039

German Edition: doi.org/10.1002/ange.202218039

Electroreduction of CO₂ on Au(310)@Cu High-index Facets

Liang Liang, Quanchen Feng, Xingli Wang,* Jessica Hübner, Ulrich Gernert, Marc Heggen, Longfei Wu, Tim Hellmann, Jan P. Hofmann, and Peter Strasser*

Abstract: The chemical selectivity and faradaic efficiency of high-index Cu facets for the CO₂ reduction reaction (CO₂RR) is investigated. More specifically, shape-controlled nanoparticles enclosed by Cu {hk0} facets are fabricated using Cu multilayer deposition at three distinct layer thicknesses on the surface facets of Au truncated ditetragonal nanoprisms (Au DTPs). Au DTPs are shapes enclosed by 12 high-index {310} facets. Facet angle analysis confirms DTP geometry. Elemental mapping analysis shows Cu surface layers are uniformly distributed on the Au {310} facets of the DTPs. The 7 nm Au@Cu DTPs high-index {hk0} facets exhibit a CH₄:CO product ratio of almost 10:1 compared to a 1:1 ratio for the reference 7 nm Au@Cu nanoparticles (NPs). *Operando* Fourier transform infrared spectroscopy spectra disclose reactive adsorbed *CO as the main intermediate, whereas CO stripping experiments reveal the high-index facets enhance the *CO formation followed by rapid desorption or hydrogenation.

The renewable electricity-powered, direct electrochemical conversion of CO₂ and water into hydrocarbon and oxygenate products constitutes a promising approach towards carbon-neutral fuels and chemicals.^[1] However, this technol-

ogy is currently hampered by a lack of sufficiently selective and efficient electrochemical catalysts.^[2] Cu catalysts are unique in converting CO₂ into hydrocarbons, such as synthetic methane, mainly because of their balanced CO binding strength and stabilization of key reactive intermediates.^[3] Synthetic methane (CH₄) is an appealing carbon-neutral energy carrier, as the liquefied and pipeline based CH₄ chain is mature and cost-effective.^[4] Also, a synthetic methane-based future residential heating infrastructure is greatly preferred over a hydrogen-based one, due to vast technology adaption cost and safety concerns. Increasing effort has been directed towards fabricating Cu-based catalyst systems with well-defined facet and morphology structures for understanding the CO₂ selective reduction process. Among these structurally well-defined Cu-based model catalysts, facet-dependent structural selectivity has been widely studied on low-index Cu facets. Hori and co-workers^[5] performed CO₂ reduction using chronopotentiometry at -5 mA cm^{-2} in an aqueous KHCO₃ electrolyte. Cu(100) and Cu(111) surfaces favored the formation of C₂H₄ and CH₄, respectively, while Cu(110) promoted the production of acetate and acetaldehyde. Subsequently, Buonsanti et. al^[6] observed an increasing level of ethylene FE for Cu cubes enclosed with {100} facets, while Cu octahedra enclosed with {111} facets reached a CH₄ selectivity of up to 51%. Recently, Koper and co-workers^[7] utilized online electrochemical mass spectrometry (OLEMS) to monitor CO reduction products (CH₄ and C₂H₄) on Cu single-crystal surfaces, confirming that C₂H₄ formation is favored on Cu(100), while CH₄ and C₂H₄ evolved simultaneously on Cu(111). The low-index facet effect of Cu on CO₂ reduction electrocatalysis has been well documented in the literature.

By contrast, the catalytic reactivity of high-index Cu facets, in particular in the form of shape- and facet-controlled nanocrystals, has remained often unexplored.^[8] Direct synthesis of high-index noble metal facets through the growth of well-shaped gold templates has been demonstrated before, but the synthesis of non-noble high-index Cu facets other than the above remains a challenge.^[9] The most prominent feature of high-index facets is that there exists a high density of surface steps and kinks with low coordination.^[10] These steps or kinks can enhance bond breaking and making through sharply varying surface-binding energies of adsorbates, which, in turn, changes the reaction pathway toward different products.^[11] However, according to the Wulff construction rule,^[12] high-index facets are energetically unfavorable, which implies that they reconstruct back to lower-index facets. Several literatures

[*] L. Liang, Q. Feng, X. Wang, J. Hübner, L. Wu, Prof. P. Strasser
 Department of Chemistry, Chemical Engineering Division, Technical University Berlin
 Straße des 17. Juni 124, 10623 Berlin (Germany)
 E-mail: xingli.wang@tu-berlin.de
 pstrasser@tu-berlin.de

U. Gernert
 Institutes of Physical Science and Information Technology, Center for Electron Microscopy (ZELMI), Technical University Berlin
 Straße des 17. Juni 124, 10623 Berlin (Germany)

M. Heggen
 Ernst Ruska-Centre for Microscopy and Spectroscopy with Electrons, Forschungszentrum Jülich GmbH
 52425 Jülich (Germany)

T. Hellmann, Prof. J. P. Hofmann
 Surface Science Laboratory, Department of Materials and Earth Sciences, Technical University of Darmstadt
 Otto-Berndt-Straße 3, 64287 Darmstadt (Germany)

© 2023 The Authors. Angewandte Chemie International Edition published by Wiley-VCH GmbH. This is an open access article under the terms of the Creative Commons Attribution License, which permits use, distribution and reproduction in any medium, provided the original work is properly cited.

reported the fabrication of Cu film with high-index facets,^[8,13] which are always inevitably affected by grain boundary effects and grain size effects, the relationship between facets and CO₂RR performance has thus far remained elusive. Therefore, new preparation strategies towards epitaxially grown, high-index Cu facets that are stabilized by highly durable, facet-controlled metallic substrates holds the key to better understand the molecular reaction mechanism and the selectivity of CO₂ reduction on facet controlled nanostructured particles.

Here, we report the successful synthesis of nanostructured shape-controlled Au/Cu core-shell model particles with all {hk0} high-index Cu facets. The facets are generated by deposition of Cu layers on precisely controlled {310} high-index Au facets that enclose a very specific ditetragonal prism-shaped Au nanocrystal (Au DTP). Owing to the high surface energy and high density of surface steps and kinks, the high-index Cu facets expose large fractions of low-coordinated surface atoms, which catalyze the CO₂ reduction with unique selectivity,^[14] see Figure 1. We characterize the electrocatalytic behavior and correlate it to reactive surface intermediates using operando electrochemical FTIR spectroscopy. We uncover distinct variations in surface coverage of specific reactive adsorbates relative to a spherical/cuboctahedral Au-Cu core-shell reference catalysts. The present communication is to spark wider synthetic and kinetic experimental and computational efforts to uncover and control CO₂ reduction reaction (CO₂RR) on high energy, high-index Cu facets.

Cu multilayers were deposited on top of truncated Au ditetragonal nanoprisms (DTPs)—nanocrystals that are precisely enclosed by 12 high-index {310} facets—at three distinct controlled thicknesses. To achieve this, pure Au DTPs with 12 high-index {310} facets were synthesized first.^[15] Scanning electron microscopy (SEM) images (Fig-

ure S1A) of the Au nanoparticles (NPs) showed the characteristic truncated ditetragonal prism morphology with average size of about 200–400 nm. Energy-dispersive X-ray spectroscopy (EDX) spectra in Figure S1B confirmed the purity of synthesized Au DTPs. Au DTPs were unambiguously identified using their TEM images (Figure 2A) and the corresponding four-fold symmetrical selected area electron diffraction (SAED) pattern (Figure 2A, inset) that evidenced characteristic facet angles along the [001] direction of $\alpha = 143.6^\circ$ and $\beta = 126.5^\circ$, respectively, which are very close to the theoretical mathematical values of Au {310} ($\alpha = 143.1^\circ$ and $\beta = 126.9^\circ$, Figure 2B, and Movie S1).^[16] The FT-IR spectroscopy spectra of Au DTPs in Figure S2 demonstrated the absence of poly(diallyldimethylammonium chloride), giving direct evidence for the formation of clean Au DTPs. Subsequently, as shown in Figure S3, the Au DTPs underwent a controlled Cu atom electrodeposition process at -0.2 V, -0.3 V and -0.4 V vs. Ag/AgCl, yielding Cu layer-by-layer growth with thickness of 4.50 nm, 6.74 nm and 9.76 nm (Table S1), respectively (denoted as 5 nm-thick Au@Cu DTPs, 7 nm-thick Au@Cu DTPs, and 10 nm-thick Au@Cu DTPs). SEM images in Figure 2C feature their 2D overlayer morphology with a lateral size of ca. 300 nm, evidencing absence of 3D island growth. EDX mappings in Figure 2D–F, S4–6 showed a homogeneous Cu surface coverage on the Au DTPs, confirming the Cu deposited along the Au {310} facets. X-ray photoelectron spectroscopy (XPS) spectra for 7 nm Au@Cu DTPs in Figure S7 identified the ratio of Cu and Au was $\approx 3:1$, higher than the nominal ratio of 1:5, which evidenced the overlayer nature of Cu on top of Au. We note that the slightly uneven projected thickness of Cu layer in Figure S5C could be attributed to the small tilt angle away from the zone axis orientation. As the deposition potential increased, there were small Cu particles discernible at the 10 nm-thick Au@Cu DTPs (Figure S6C). For comparison and reference, 300 nm spherical/cuboctahedral Au NPs covered with a similar amount of copper layers were

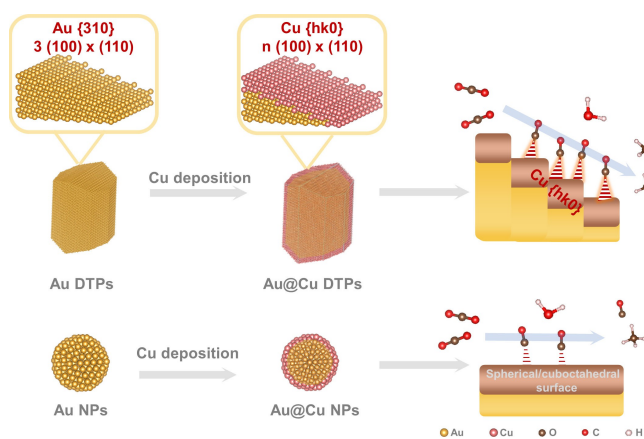


Figure 1. Schematic representation of the possible catalytic mechanism of selective CO₂ electroreduction to CH₄ over shape- and morphology-controlled {hk0} facets of Au@Cu DTP catalysts, and non-shape controlled, spherical/cuboctahedral Au@Cu reference catalyst NPs, respectively, of comparable size. The {hk0} facets are periodically constituted of $n \times (100)$ as terrace and one (110) as step, i.e. $n (100) \times (110)$, while the non-shape controlled spherical/cuboctahedral surface composes of differently orientated facets.

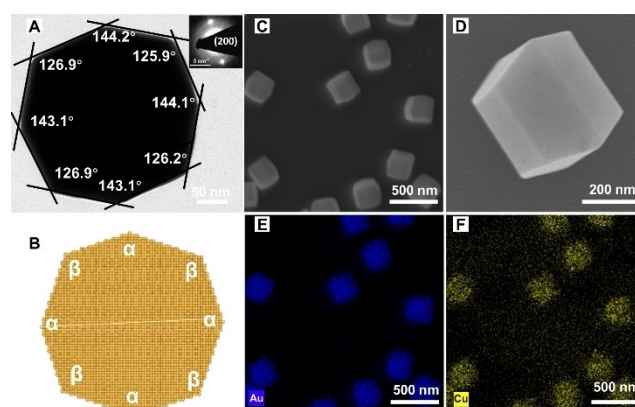


Figure 2. Characterization of the {310} Au facets and {hk0} Cu facets. (A) TEM image (inset: the corresponding SAED pattern) and (B) model illustration for the Au DTPs; the line connecting the Bragg reflections indicate the location of α angles; (C–D) HR-SEM, and (E–F) corresponding EDX mapping images of 7 nm-thick Au@Cu DTPs.

synthesized, denoted as 5 nm-thick Au@Cu NPs, 7 nm-thick Au@Cu NPs, 10 nm-thick Au@Cu NPs (Figures S8–10, table S1). Our synthesis and characterization unequivocally confirmed the successful formation of core–shell Au/Cu DTPs (here referred to as Au@Cu DTPs), covered by Cu multi-layers with controlled facet orientation.

To investigate the CO₂ electrocatalysis of Cu {hk0} facets, activity and efficiency tests of CO₂ electroreduction were conducted for all Au@Cu DTPs, and compared to those done with spherical/cuboctahedral Au@Cu NPs. The CO₂ reduction activity was tested on a glassy carbon electrode (GCE) using an H-cell with a catalyst loading of 0.15 mg cm⁻². As shown in Figure 3A–F and S11, both the Au@Cu DTPs and spherical/cuboctahedral Au@Cu NPs realized CO₂ reduction into C₁ products and a small amount of C₂ products (ethylene and ethanol), in which the predominant products were CO and CH₄ accompanied with a small amount of formic acid. Intriguingly, 7 nm-thick Au@Cu DTPs showed a CH₄:CO ratio of almost 10:1 compared to the roughly 1:1 ratio for the spherical/cuboctahedral 7 nm-thick Au@Cu NPs at ≈ -0.96 V vs. RHE (Figure 3B and E). The 7 nm-thick Au@Cu DTPs showed CO₂RR performance resembling the data on single crystal (310) and (210) surfaces in Hori and Bagger's work,

respectively.^[14,17] This is because the thickness of the Cu layer results in a partial facet relaxation of surface Cu atoms, narrowing the (100) terraces near the surface. While the exposed facets continue to be {hk0} facets, they showed an increased ratio of Cu(210) facets. Cu(210) facets not only showed a similar surface energy as Cu(310) ones, but also possessed identical angles for the octagons along [001] direction, with simply α and β angles exchanged (Figure S12).^[17] Besides, the growth of Cu had a crystalline order directed by the Au (310) substrate, it is likely that the oriented growth has propagated through each layer and is still apparent on the surface, which could exclude the formation of the polycrystalline Cu layers.^[18] Moreover, at ≈ -0.96 V vs. RHE, the faradaic selectivity in Figure S13 for CH₄ of 25.36% for 7 nm-thick Au@Cu DTPs was roughly 4 times larger than that of spherical/cuboctahedral 7 nm-thick Au@Cu NPs (6.27%). Furthermore, the 7 nm-thick Au@Cu DTPs presented roughly 1.4-fold higher faradaic efficiency of CH₄ relative to the 5 nm-thick Au@Cu DTPs (Figure 3A–B), because the thicker Cu layer could help to retain more stable Cu surface facets. The 10 nm catalyst showed a similar FE of CH₄ in Figure 3B as the 7 nm thick film because at this point the thickness was not the only impact factor, but the existence of small Cu particles discernible at the 10 nm-thick Au@Cu DTPs could also affect the selectivity of performance. For comparison, there was no obvious selectivity trend for the Cu-covered spherical/cuboctahedral Au nanoparticles at any thickness, suggesting absence of preferred facet selectivity due to the more isotropic structure and low-facet distribution (Figure 3D–F). Consequently, the higher index Cu{hk0} facets enhanced the CO₂-to-CH₄ selectivity through a structure sensitivity effect.

To understand how the high-index Cu {hk0} facets enhance the catalytic CO₂-to-CH₄ selectivity and activity, operando Fourier transform infrared spectroscopy (FT-IR) was carried out to gain insights into the key intermediates over the high-index Cu {hk0} facets. As shown in Figure 4A, no obvious peaks were detected at rather anodic electrode potentials near -0.1 V_{RHE}, prior to CO₂ electrolysis. Then, the band at 2100 cm⁻¹ was assigned to the reactive linear *CO intermediate, gradually appeared and strengthened with electrolysis time.^[19] In addition, no red shift of *CO

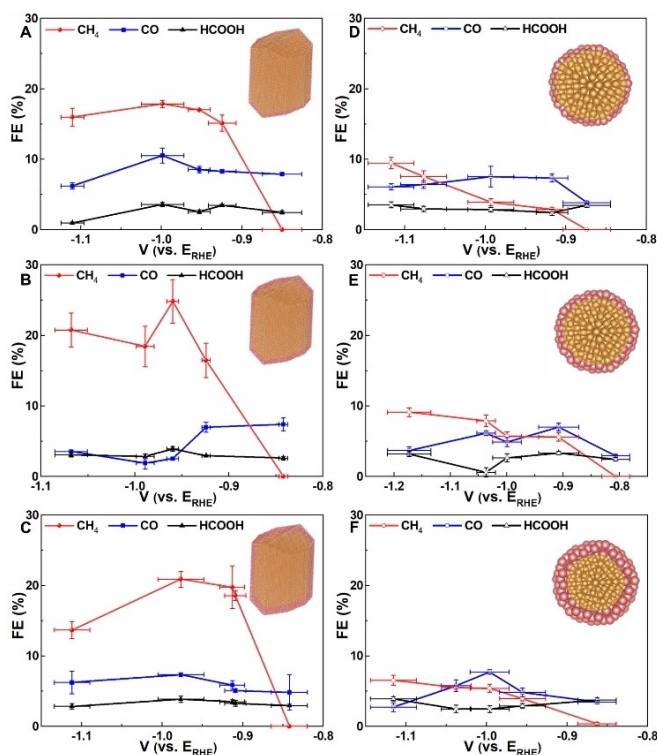


Figure 3. CO₂ electroreduction faradaic efficiencies of {hk0} Cu facets versus spherical/cuboctahedral Cu nanoparticles as function of overlayer thickness. Faradaic efficiency for (A) 5 nm-thick Au@Cu DTPs, (B) 7 nm-thick Au@Cu DTPs, (C) 10 nm-thick Au@Cu DTPs, (D) 5 nm-thick Au@Cu NPs, (E) 7 nm-thick Au@Cu NPs, (F) 10 nm-thick Au@Cu NPs, respectively. (inset: the corresponding model illustration for the Au@Cu DTPs and Au@Cu NPs with various thickness, respectively.)

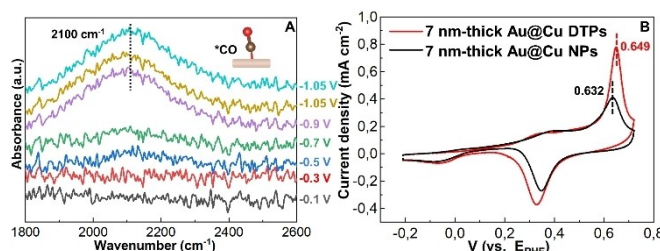


Figure 4. Operando characterizations and experimental mechanistic studies of {hk0} Cu facets versus spherical/cuboctahedral Cu nanoparticles. (A) Operando FTIR spectra of the 7 nm-thick Au@Cu DTPs recorded at different potential intervals (inset: model illustration for the adsorbed *CO on the Au@Cu DTPs). (B) Cyclic Voltammograms (CVs) recorded in 0.1 M KOH with CO-saturated electrolyte for the 7 nm-thick Au@Cu DTPs and the 7 nm-thick Au@Cu NPs, respectively.

bands were observed by the FT-IR spectra in Figure 4A. *CO protonation to *CHO is widely accepted the key step for methane formation, and the simultaneous suppression of both HER and C–C coupling is the key to boost methane selectivity. If *CO intermediates involved in the C–C coupling process, the position of *CO would be red shifted to lower frequencies due to the stronger interaction between *CO and the surface of the catalyst, which promotes CO dimerization. These findings indicate and account for the dominant *CO protonation process to methane. To further investigate the binding affinity of adsorbed *CO on the Cu multilayers of varying thickness deposited on the Au DTPs and spherical/cuboctahedral Au nanoparticles, molecular CO oxidation experiments were conducted by oxidative LSV stripping scans under a CO-saturated 0.1 M KOH electrolyte.^[20] The results in Figure 4B revealed increased CO stripping currents and charges for the 7 nm-thick Au@Cu DTPs as compared to the spherical/cuboctahedral 7 nm-thick Au@Cu NPs. Meanwhile, the stripping peak potential of adsorbed *CO adsorption on the 7 nm-thick Au@Cu DTPs was 0.649 V, more anodic of that of the spherical/cuboctahedral 7 nm-thick Au@Cu spherical/cuboctahedral NPs (0.632 V). The increased current density and the higher peak potential of the 7 nm-thick Au@Cu DTPs suggest stronger chemisorption of *CO on the facet controlled Cu surface, which, in turn, facilitates subsequent *CO hydrogenation via proton-coupled electron transfer.^[21] Consequently, the Cu {hk0} facets not only favored the formation of the *CO intermediate, but also exhibited stronger *CO binding energy as compared to spherical/cuboctahedral Au@Cu NPs, which thereby reasonably accounts for the enhanced CO₂-to-CH₄ pathway.

In conclusion, this communication reports the electrocatalytic activity and selectivity for CO₂ electroreduction of high index Cu facets exposed on shape-controlled nanoparticles. High-index nanoparticle Cu facets—synthetically challenging to realize for pure Cu nanoparticles—were synthesized using galvanic deposition of atomic Cu layers of varying thicknesses on precisely facet- and shape controlled Au DTP nanoparticles (Au@Cu DTPs). Cu overlayers of identical thickness on non shape-controlled spherical/cuboctahedral Au nanoparticles served as reference catalysts. Au@Cu DTPs were enclosed by 12 high-index Cu {hk0} facets. EDX mapping image indicated Cu was homogeneously deposited along the Au {310} facets.

Owing to the exposure of Cu {hk0} high-index facets, 7 nm-thick Au@Cu DTPs showed a CH₄:CO ratio of almost 10:1 compared to the roughly 1:1 ratio for the isotropic structure of spherical/cuboctahedral 7 nm-thick Au@Cu NPs. Moreover, the 7 nm-thick Au@Cu DTPs presented roughly 1.4-fold higher faradaic efficiency of CH₄ relative to the 5 nm-thick Au@Cu DTPs, indicating the thicker {hk0} Cu layer helped improved CH₄ production.

Operando FT-IR spectra and CO stripping experiments illustrated that the high index Cu facets favor *CO formation and hydrogenation, which accounts for the higher faradic efficiency for hydrocarbons. This study manifests the feasibility of high-index facets engineering to drive specific CO₂-to-chemicals or fuels reaction channels.

Acknowledgements

This work was financially supported by the European Union's Horizon 2020 research and innovation programme under grant No. 101006701, EcoFuel, and the Deutsche Forschungsgemeinschaft (DFG, German Research Foundation, grant No. STR 596/18-1 and LI 4184/2-1), and the Initiative and Networking Fund of the Helmholtz Association (grant agreement No. KA2-HSC-12, 'A Comprehensive Approach to Harnessing the Innovation Potential of Direct Air Capture and Storage for Reaching CO₂-Neutrality', DACStorE). We acknowledge the fellowship from the International Postdoc Initiative (IPODI) of the Technische Universität Berlin. We also thank Dipl. Ing. Sören Selve from Zentraleinrichtung für Elektronenmikroskopie (ZELMI) of the Technical University Berlin for the support with TEM-EDX mapping measurements. Q. F. gratefully acknowledges the support from Alexander von Humboldt Foundation. Open Access funding enabled and organized by Projekt DEAL.

Conflict of Interest

The authors declare no conflict of interest.

Data Availability Statement

The data that support the findings of this study are available from the corresponding author upon reasonable request.

Keywords: Electromethanation · High-Index Cu Facets · Operando Fourier Transform Infrared Spectroscopy

- [1] D. Tong, Q. Zhang, Y. Zheng, K. Caldeira, C. Shearer, C. Hong, Y. Qin, S. J. Davis, *Nature* **2019**, *572*, 373–377.
- [2] C. T. Dinh, T. Burdyny, M. G. Kibria, A. Seifitokaldani, C. M. Gabardo, F. P. G. de Arquer, A. Kiani, J. P. Edwards, P. De Luna, O. S. Bushuyev, C. Q. Zou, R. Quintero-Bermudez, Y. J. Pang, D. Sinton, E. H. Sargent, *Science* **2018**, *360*, 783–787.
- [3] S. Nitopi, E. Bertheussen, S. B. Scott, X. Y. Liu, A. K. Engstfeld, S. Horch, B. Seger, I. E. L. Stephens, K. Chan, C. Hahn, J. K. Nørskov, T. F. Jaramillo, I. Chorkendorff, *Chem. Rev.* **2019**, *119*, 7610–7672.
- [4] X. Wang, P. F. Ou, J. Wicks, Y. Xie, Y. Wang, J. Li, J. Tam, D. Ren, J. Y. Howe, Z. Y. Wang, A. Ozden, Y. Z. Finckel, Y. Xu, Y. H. Li, A. S. Rasouli, K. Bertens, A. H. Ip, M. Graetzel, D. Sinton, E. H. Sargent, *Nat. Commun.* **2021**, *12*, 3387.
- [5] Y. Hori, H. Wakebe, T. Tsukamoto, O. Koga, *Surf. Sci.* **1995**, *335*, 258–263.
- [6] G. L. De Gregorio, T. Burdyny, A. Loiudice, P. Iyengar, W. A. Smith, R. Buonsanti, *ACS Catal.* **2020**, *10*, 4854–4862.
- [7] K. J. P. Schouten, Y. Kwon, C. J. M. van der Ham, Z. Qin, M. T. M. Koper, *Chem. Sci.* **2011**, *2*, 1902–1909.
- [8] C. Hahn, T. Hatsukade, Y. G. Kim, A. Vailionis, J. H. Baricauat, D. C. Higgins, S. A. Nitopi, M. P. Soriaga, T. F. Jaramillo, *Proc. Natl. Acad. Sci. USA* **2017**, *114*, 5918–5923.
- [9] F. Wang, C. Li, L. Sun, H. Wu, T. Ming, J. Wang, J. C. Yu, C. Yan, *J. Am. Chem. Soc.* **2011**, *133*, 1106–1111.

- [10] C. Xiao, B. A. Lu, P. Xue, N. Tian, Z. Y. Zhou, X. Lin, W. F. Lin, S. G. Sun, *Joule* **2020**, *4*, 2562–2598.
- [11] a) C. Shi, H. A. Hansen, A. C. Lausche, J. K. Norskov, *Phys. Chem. Chem. Phys.* **2014**, *16*, 4720–4727; b) C. Chang, M. Ku, *J. Phys. Chem. C* **2021**, *125*, 10919–10925; c) Z. Wang, G. Yang, Z. Zhang, M. Jin, Y. Yin, *ACS Nano* **2016**, *10*, 4559–4564.
- [12] Y. G. Sun, Y. N. Xia, *Science* **2002**, *298*, 2176–2179.
- [13] a) M. Philip, A. R. Woldu, M. B. Akbar, H. Louis, H. Cong, *Nanoscale* **2021**, *13*, 3042–3048; b) J. Y. Kim, W. Park, C. Choi, G. Kim, K. M. Cho, J. Lim, S. J. Kim, A. Al-Saggaf, I. Gereige, H. Lee, W. Jung, Y. Jung, H. Jung, *ACS Catal.* **2021**, *11*, 5658–5665; c) H. Zhang, C. He, S. Han, Z. Du, L. Wang, Q. Yun, W. Cao, B. Zhang, Y. Tian, Q. Lu, *Chin. Chem. Lett.* **2022**, *33*, 3641–3649.
- [14] A. Bagger, W. Ju, A. S. Varela, P. Strasser, J. Rossmeisl, *ACS Catal.* **2019**, *9*, 7894–7899.
- [15] F. S. Ke, B. Solomon, Y. Ding, G. L. Xu, S. G. Sun, Z. L. Wang, X. D. Zhou, *Nano Energy* **2014**, *7*, 179–188.
- [16] F. Lu, Y. Zhang, L. H. Zhang, Y. G. Zhang, J. X. Wang, R. R. Adzic, E. A. Stach, O. Gang, *J. Am. Chem. Soc.* **2011**, *133*, 18074–18077.
- [17] Y. Hori, I. Takahashi, O. Koga, N. Hoshi, *J. Phys. Chem. B* **2002**, *106*, 15–17.
- [18] M. V. Kelso, J. Z. Tubbesing, Q. Chen, J. A. Switzer, *J. Am. Chem. Soc.* **2018**, *140*, 15812–15819.
- [19] a) B. L. Mojat, S. D. Ebbesen, L. Lefferts, *Chem. Soc. Rev.* **2010**, *39*, 4643–4655; b) A. Wuttig, C. Liu, Q. L. Peng, M. Yaguchi, C. H. Hendon, K. Motobayashi, S. Ye, M. Osawa, Y. Surendranath, *ACS Cent. Sci.* **2016**, *2*, 522–528; c) O. Krauth, G. Fahsold, N. Magg, A. Pucci, *J. Chem. Phys.* **2000**, *113*, 6330–6333.
- [20] A. Auer, M. Andersen, E. M. Wernig, N. G. Hormann, N. Buller, K. Reuter, J. Kunze-Liebhauser, *Nat. Catal.* **2020**, *3*, 797–803.
- [21] a) D. F. Gao, H. Zhou, J. Wang, S. Miao, F. Yang, G. X. Wang, J. G. Wang, X. H. Bao, *J. Am. Chem. Soc.* **2015**, *137*, 4288–4291; b) J. F. Zhang, K. D. Li, B. Zhang, *Chem. Commun.* **2015**, *51*, 12012–12015; c) T. Vidakovic, M. Christov, K. Sundmacher, *Electrochim. Acta* **2007**, *52*, 5606–5613.

Manuscript received: December 7, 2022

Accepted manuscript online: January 19, 2023

Version of record online: February 8, 2023